



Mechanism of carbon deposits removal from supported Ni catalysts

Stavros Alexandros Theofanidis^a, Vladimir V. Galvita^{a,*}, Hilde Poelman^a, Rakesh Batchu^a, Lukas C. Buelens^a, Christophe Detavernier^b, Guy B. Marin^a

^a Laboratory for Chemical Technology, Ghent University, Technologiepark 914, B-9052 Ghent, Belgium

^b Department of Solid State Sciences, Ghent University, Krijgslaan 281, S1, B-9000 Ghent, Belgium

ARTICLE INFO

Keywords:

Catalyst deactivation
Catalyst regeneration
Carbon removal
Metal particle migration

ABSTRACT

Catalyst deactivation due to carbon deposition is a major issue in all reforming technologies. Because of the significant economic cost of catalyst replacement, catalyst regeneration is increasingly attracting attention. The regeneration mechanism of Ni catalysts, with respect to carbon removal, was investigated on support materials prepared by one-pot synthesis. The supports were classified based on their redox functionality: Al_2O_3 , MgAl_2O_4 show no redox properties in contrast to $\text{MgFe}_{0.09}\text{Al}_{1.91}\text{O}_4$ and CeZrO_2 that have redox functionality.

A Temporal Analysis of Products (TAP) setup was used to investigate the isothermal regeneration mechanism of Ni catalysts at 993 K by O_2 . Different mechanisms were distinguished depending on the redox functionality of the support material. Two consecutive steps occur on the support that have no redox properties (Al_2O_3 and MgAl_2O_4): metallic Ni is oxidized to form NiO (oxidation step), resulting in an initial local temperature increase of 50–60 K in total, enabling metal particle migration to carbon that was initially separated from the metal and subsequent oxidation through NiO lattice oxygen (reduction step). On the other hand, the mechanism of carbon removal by O_2 from Ni catalysts on supports with redox properties does not require particle migration. Two parallel contributions are proposed: 1) Ni metal is oxidized to form NiO, where after lattice oxygen of NiO is used for the oxidation of carbon that is deposited upon the metals, 2) carbon oxidation through lattice oxygen that is provided by the support. No dependency of the carbon gasification mechanism on the exposed fraction of the metal (particle size in the nanoscale) or on the structure of the deposited carbon was concluded.

1. Introduction

Syngas is a building block for chemical industry and it is the product of all the reforming technologies [1]. One of the main challenges, common to reforming processes, as well as to methanation and steam cracking of hydrocarbons [2,3], is carbon formation [4]. In catalytic reforming, it will lead to catalyst deactivation and thus process shutdown, resulting in a major economic cost [5].

Catalyst regeneration is eventually required, by removing all carbon species through gasification [6,7]. Oxygen is one of the gases most often used for gasification [8] in order to infer type and location of carbon species on the catalyst, while there are also studies on carbon gasification by CO_2 , H_2O and H_2 [9–13]. The rate of carbon gasification is a function of its structure [14], location [15] and of the nature of the catalyst present [16–18]. Temperature programmed (TP) techniques are important for carbon species characterization [19,20]. However, isothermal studies are also required in order to understand and model the kinetics [7].

Different mechanisms for catalyst regeneration from carbon deposits have been proposed since the 1930s, including increased adsorption of the oxidizing gas (CO_2 or H_2O) [21] and mobility of valence electrons from the catalyst lattice to carbon [22]. Wood [23] suggested that particularly for alkali metal catalysts, a liquid film that wets the carbon surface is formed. The molten catalyst layer, which is an oxygen deficient compound, attacks during gasification the carbon surface. Other available mechanisms in literature include: 1) carbon bulk diffusion that was suggested in the 1980s, where carbon is transported through the metal particle to the region where the gasification reaction takes place [9,4], 2) oxygen/hydrogen spillover, where metal-activated oxygen/hydrogen migrates over a considerable distance on the support towards the deposited carbon species to remove them [10], and 3) the redox mechanism, where the catalyst provides lattice oxygen to carbon (reduction step) and is then oxidized by a gas phase oxidizer (O_2 , CO_2 , H_2O ; oxidation step) [24,25]. A fourth mechanism has recently been proposed, which includes mobility of the active metal particles [13] towards the carbon deposits, when O_2 is used as gasification agent due

* Corresponding author.

E-mail address: Vladimir.Galvita@UGent.be (V.V. Galvita).

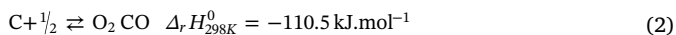
<https://doi.org/10.1016/j.apcatb.2018.08.042>

Received 12 June 2018; Received in revised form 10 August 2018; Accepted 17 August 2018

Available online 18 August 2018

0926-3373/© 2018 Elsevier B.V. All rights reserved.

to the exothermicity of the reactions (Eqs. (1) and (2)). Then, the deposited carbon is removed via the redox mechanism.



The mobility of metal particles on graphite under O_2 and CO_2 atmosphere was evidenced in 1964 [26]. Later, McKee used hot stage optical microscopy to demonstrate mobility of catalytic particles with channeling on graphite [27]. Transition metal particles may engage in transport through the layers of carbon deposits during carbon gasification by O_2 [28–30]. The atoms of solid surfaces become mobile due to thermal energy at temperatures well below the melting point. The mobility temperature of various metal and metal oxide particles dispersed on graphite was investigated by Baker [31]. By comparing this specific temperature with the melting point of different particles (Ag, Au, Cu, Ni, Pd, Co, Fe, Pt, ...), Baker found that the mobility temperature coincided with the Tammann temperature of these materials. In a recent review [32], Lobo and Carabineiro compared the several available mechanisms in literature for carbon gasification. They indicated the success of the carbon bulk diffusion mechanism in explaining the observed kinetic and geometry effects.

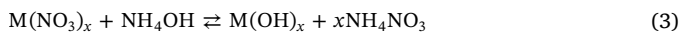
There have been many attempts to reach a concluding mechanism for catalyst regeneration from carbon deposits, but so far no unambiguous conclusion has been reached. The present work aims at elucidating this question by means of dedicated isothermal regeneration experiments on Ni reforming catalysts. Different parameters are varied: support material, exposed fraction of the active metals at the nanoscale, structure of the deposited carbon and type of active metal. A transient technique, Temporal Analysis of Products (TAP), is used to investigate the isothermal carbon species gasification process using oxygen as regeneration agent. The TAP reactor is an important tool for investigating heterogeneous reactions, particularly reactions on industrial catalysts. The high time resolution of the TAP technique allows detection of short- (millisecond time scale) and/or long-lived (> 1 s) reaction intermediates, which helps to formulate the reaction mechanism [33–35].

2. Experimental methods

2.1. Support and catalyst preparation

2.1.1. Support preparation

One-pot synthesis by co-precipitation was applied for the support materials: Al_2O_3 , MgAl_2O_4 , $\text{MgFe}_x\text{Al}_{2-x}\text{O}_4$ ($x = 0.09$) and CeZrO_2 . The precursors, $\text{Al}(\text{NO}_3)_3 \cdot 9\text{H}_2\text{O}$ (98.5%, Sigma-Aldrich®), $\text{Mg}(\text{NO}_3)_2 \cdot 6\text{H}_2\text{O}$ (99%, Sigma-Aldrich®), $\text{Fe}(\text{NO}_3)_3 \cdot 9\text{H}_2\text{O}$ (99.99 + %, Sigma-Aldrich®), $\text{Ce}(\text{NO}_3)_3 \cdot 6\text{H}_2\text{O}$ and ZrN_2O_7 were dissolved in water. A precipitating agent, NH_4OH (ACS reagent, 28.0 – 30.0% NH_3 basis), was added to adjust the pH to 10, at 333 K, forming the corresponding hydroxides (Eq. (3)). The produced precipitate containing the hydroxides was filtered, dried at 393 K for 12 h, and subsequently calcined in air at 1023 K for 4 h, leading to the formation of the oxide support materials.



where M = Al, Mg, Ce, Fe.

The supports were chosen according to their different properties and can be ranked in two categories, supports with and without redox properties. Al_2O_3 and MgAl_2O_4 show no or little oxygen mobility compared to $\text{MgFe}_x\text{Al}_{2-x}\text{O}_4$ [36,37] and CeZrO_2 [38,39].

2.1.2. Catalyst preparation

Monometallic 9 wt%Ni catalysts were prepared by incipient wetness impregnation on the aforementioned supports (Al_2O_3 , MgAl_2O_4 , $\text{MgFe}_x\text{Al}_{2-x}\text{O}_4$ and CeZrO_2) using an aqueous solution of $\text{Ni}(\text{NO}_3)_2 \cdot 6\text{H}_2\text{O}$ (99.99 + %, Sigma-Aldrich®). The catalysts were dried at 393 K for 12 h

and subsequently calcined in air at 1023 K for 4 h, resulting in “as-prepared” catalysts. Also, a 1 wt% Rh sample was synthesized on a MgAl_2O_4 support for comparison purposes.

2.2. Support and catalyst characterization

The Brunauer-Emmett-Teller (BET) surface area of each sample was determined by N_2 adsorption at 77 K (five point BET method using Tristar Micromeritics) after outgassing the sample at 473 K for 2 h. The bulk chemical composition of support and as-prepared catalysts was determined by means of inductively coupled plasma atomic emission spectroscopy (ICP-AES, ICAP 6500, Thermo Scientific). The samples were mineralized by acid fusion.

2.3. Catalyst coking protocol

The coking of the catalyst was performed 1) at atmospheric pressure in a quartz reactor with an internal diameter of 9 mm, which was housed inside an electric furnace and 2) by pulsing CH_4 in the TAP reactor set-up.

For the experiments performed in the quartz reactor, the purpose was to deposit carbon on the catalysts prior to carbon gasification. DRM at 1023 K was chosen as a reforming reaction to coke the catalysts in a continuous flow experiment, where the CH_4/CO_2 ratio was equal to 2/1. The temperature of the catalyst bed was measured with N-type thermocouples touching the outside and inside of the reactor at the position of the catalyst bed. The inlet gas flow rates were always maintained by means of calibrated Bronkhorst mass flow controllers. Prior to each coking experiment, the fresh sample was reduced in a 1 N mL s^{-1} flow of 30 vol% H_2/Ar at 1123 K for 30 min and then the flow was switched to Ar for 30 min.

Transient measurements were performed in a TAP-3E reactor (Mithra Technologies, St. Louis, USA) equipped with an Extrel Quadrupole Mass Spectrometer (QMS). The details of the TAP reactor can be found in [33]. For the experiments, 20 mg ($250 < d_{\text{particle}} < 500 \mu\text{m}$ catalyst fraction) of the catalyst was placed in a quartz microreactor (I.D = 4 mm and ~ 2 mm bed length), which was located between two inert beds of quartz particles with the same sieved fraction. The temperature of the catalyst was measured by a K-type thermocouple housed inside the catalytic zone. The following procedure was applied for coking the catalysts by pulsing CH_4 in the TAP reactor set-up (Fig. S1): (a) the samples were pre-reduced in a continuous flow setup using a quartz reactor under flow of 1 mL s^{-1} of 30 vol% H_2/Ar at 1123 K, using a heating ramp of 15 K min^{-1} and a dwell time of 30 min at 1123 K. The catalysts were cooled down under Ar flow and then immediately placed in the TAP reactor, named as “reduced”. (b) H_2 pulses were initially applied, after placing the catalyst in the TAP reactor, to ensure that it was fully reduced. (c) A series of CH_4 pulses, diluted in Ar, (approximately 10^{-7} mol/pulse) were used isothermally at 993 K for coking (carbon deposition) of the catalysts, yielding an “coked catalyst” state. Ar was used as internal standard. H_2 , CH_4 , H_2O , CO , O_2 , Ar and CO_2 responses were monitored at amu signals of respectively 2, 16, 18, 28, 32, 40 and 44 by QMS. Data were recorded with millisecond time resolution in each pulse. A correction was applied to remove contributions from unavoidable interference with fragmentation peaks of other gases. The average amount of CH_4 that was pulsed during catalyst coking was $4 \cdot 10^{-5}$ mol. The nature of the deposited carbon during CH_4 pulsing in the TAP reactor set-up is discussed in § 3.4.

2.4. Characterization of carbon deposits

The coked catalysts under continuous flow were used for carbon characterization through Raman spectroscopy and HRTEM. Raman analysis of the samples was performed on a RXN1 Raman instrument (Kaiser Optical Systems) fitted with a 532 nm laser operating at 40 mW.

Table 1Textural properties of supports and catalysts. Metal loading from ICP-AES, BET and pore volume from N₂ adsorption.

Abbreviation	Support	wt% Ni	wt% Fe	Surface area [m ² g ⁻¹]	Pore volume [cm ³ g ⁻¹]	Pore width [10 ⁻⁹ m]
Al	Al ₂ O ₃	–	–	125.7 ± 11.6	0.28 ± 0.02	6.41 ± 0.30
MgAl	MgAl ₂ O ₄	–	–	82.0 ± 4.5	0.23 ± 0.03	8.45 ± 1.10
MgFeAl	MgFe _{0.09} Al _{1.91} O ₄	–	5.8 ^a	63.7 ± 3.5 ^a	0.17 ± 0.01 ^a	7.71 ± 0.50 ^a
CeZr	CeZrO ₂	–	–	25.2 ± 3.4	0.08 ± 0.01	8.59 ± 0.12

Abbreviation	Catalyst	wt% Ni	wt% Fe	Surface area [m ² g ⁻¹]	Pore volume [cm ³ g ⁻¹]	Pore width [10 ⁻⁹ m]
Ni-Al	9Ni/Al ₂ O ₃	9.5	–	99.1 ± 8.1	0.25 ± 0.01	7.09 ± 0.04
Ni-MgAl	9Ni/MgAl ₂ O ₄	8.5	–	61.9 ± 3.3	0.17 ± 0.01	8.09 ± 0.12
Ni-MgFeAl	9Ni/MgFe _{0.09} Al _{1.91} O ₄	8.3 ^a	5.1 ^a	45.1 ± 2.7 ^a	0.13 ± 0.01 ^a	8.20 ± 0.01 ^a
Ni-CeZr	9Ni/CeZrO ₂	9.0 [°]	–	15.3 ± 1.3	0.06 ± 0.01	10.77 ± 0.35
1Ni-MgAl	1Ni/MgAl ₂ O ₄	1.0 [°]	–	31.0 ± 1.5	0.06 ± 0.01	5.03 ± 0.06

^a Value reported in [36], [°]nominal amount.

High-resolution transmission electron microscopy (HRTEM) was used for structural analysis, while EDX yielded local chemical analysis. These techniques were implemented using a JEOL JEM-2200FS, Cs-corrected microscope operated at 200 kV, which was equipped with a Schottky-type field-emission gun (FEG) and EDX JEOL JED-2300D. All samples were deposited by immersion onto a lacey carbon film on a copper support grid.

2.5. Isothermal Temporal Analysis of Products (TAP) experiments for carbon gasification

TAP was originally developed by John T. Gleaves in 1988 [40] and later modified by him in 1997 [41]. To date, a third generation TAP reactor is available. A TAP pulse response experiment consists of injecting a very small amount of gas, typically nanomoles per pulse, into a tubular fixed bed reactor that is kept under vacuum. The time-dependent exit flow rate of each gas is detected by a mass spectrometer.

A sequence of isothermal O₂ pulses at 993 K were admitted into the microreactor for carbon gasification from “coked” catalysts. CO₂ and CO responses were monitored at amu signals of 44 and 28, respectively. The latter were recorded with millisecond time scale resolution for 5–10 s collection time.

The following expressions are used to determine total oxygen conversion (X_{O₂}), oxygen uptake by the catalyst (C_{O,M}) and oxygen conversion to gas phase products (C_{CO_x}), CO and CO₂:

$$X_{O_2} = \frac{n_{in,O_2} - n_{out,O_2}}{n_{in,O_2}} \cdot 100\%, \quad (4)$$

$$\%C_{O,M_i} = \frac{2 \cdot n_{in,O_2} - (2 \cdot n_{out,O_2} + 2 \cdot n_{out,CO_2} + n_{out,CO})}{2 \cdot n_{in,O_2}} \cdot 100\% \quad \text{with } i = \text{Ni, Ni + Fe and Ni + Ce}, \quad (5)$$

$$\%C_{CO_x} = \frac{(F_{out,CO_2} + F_{out,CO})}{F_{in,O_2}} \cdot 100\% \quad x = 1, 2 \quad (6)$$

where n_{in} and n_{out} are the inlet mol pulsed in the reactor and outlet mol of gases (O₂, CO₂ and CO) detected in the outlet of the reactor, respectively.

The total energy produced per pulse of O₂ (Eq. (7)) originates from the sum of two processes: 1) metal oxidation by gas phase oxygen (Eq. (8)), which is an exothermic reaction (see Eq. (10)) and 2) carbon oxidation via lattice oxygen originating from metal oxide (Eq. (9)), which are endothermic reactions (see Eqs. (11) and (12)). The contribution of direct carbon gasification from gas phase oxygen is considered negligible at the applied temperature.

$$Q_{tot} = Q_{m.o} + Q_{C.O_L}, \quad (7)$$

with

$$Q_{m.o} = (n_{in,O_2} - n_{out,O_2}) \cdot \Delta H_{993K, Eq. 10}^0, \quad (8)$$

$$Q_{C.O_L} = (n_{out,CO_2} + n_{out,CO}) \cdot \Delta H_{993K, Eq. 11 \text{ and } 12}^0, \quad (9)$$

where Q_{tot} is the total energy (kJ/O₂ pulse) generated during carbon gasification by the aforementioned two oxidation steps, $Q_{m.o}$ (kJ/O₂ pulse) is the energy generated per pulse of oxygen during oxidation of metal (Ni) to oxide (NiO) based on Eq. (10), and $Q_{C.O_L}$ (kJ/O₂ pulse) is the heat consumed per pulse of oxygen during carbon oxidation by metal oxide lattice oxygen (Eqs. (11) and (12)). Eqs. (10) and (11) represent the elementary steps of carbon partial oxidation (Eq. (2)). n_{in,O_2} is the amount of oxygen per pulse ($\sim 10^{-7}$ mol/pulse), n_{out,O_2} is the outlet mol of oxygen and $\Delta_r H_{993K}^0$ (kJ·mol⁻¹) is the reaction enthalpy of Eqs. (10)–(12).

$$\begin{aligned} \text{Ni} + \frac{1}{2} \text{O}_2 &\rightleftharpoons \text{NiO} & \Delta_r H_{993K}^0 &= -235.3 \text{ kJ} \cdot \text{mol}^{-1}, & \Delta_r G_{993K}^0 &= -149.2 \text{ kJ} \cdot \text{mol}^{-1}, \end{aligned} \quad (10)$$

$$\begin{aligned} \text{NiO} + \text{C} &\rightleftharpoons \text{CO} + \text{Ni} & \Delta_r H_{993K}^0 &= 112.9 \text{ kJ} \cdot \text{mol}^{-1}, & \Delta_r G_{993K}^0 &= -38.3 \text{ kJ} \cdot \text{mol}^{-1}, \end{aligned} \quad (11)$$

$$\begin{aligned} 2\text{NiO} + \text{C} &\rightleftharpoons \text{CO}_2 + 2\text{Ni} & \Delta_r H_{993K}^0 &= 75.3 \text{ kJ} \cdot \text{mol}^{-1}, & \Delta_r G_{993K}^0 &= -84.6 \text{ kJ} \cdot \text{mol}^{-1}, \end{aligned} \quad (12)$$

The local temperature increase, close to metal/metal oxide particle, can then be calculated:

$$\Delta T = \frac{Q_{tot}}{m_j \cdot C_{p,j}}, \quad \text{with } j = \text{Ni, Ni + Fe, Ni + Ce}, \quad (13)$$

where m_j is the mass of active metal, Ni, Ni-Fe or Ni-Ce, used in the bed of the TAP reactor (~ 20 mg), and $C_{p,j}$ the molar heat capacity of Ni, Ni-Fe or Ni-Ce at constant pressure (J kg⁻¹ K⁻¹).

3. Results

3.1. Catalyst characterization

Table 1 shows an overview of the elemental composition of supports and catalysts obtained from ICP along with surface area, pore volume and average pore width as measured by N₂-adsorption. The incorporation of Fe into the magnesium aluminate lattice led to a decrease of surface area, 63.7 m² g⁻¹ for MgFe_{0.09}Al_{1.91}O₄ vs. 82.0 m² g⁻¹ for MgAl₂O₄, as was published elsewhere [36]. This is in agreement with Dharanipragada and co-workers [42], who observed a decrease from 90 to 30 m² g⁻¹, when the Fe content was increased from 5 wt% up to 15 wt%. The catalysts showed a lower surface area than their corresponding supports, which is attributed to surface covering and pore blocking of support caused by Ni impregnation, similar to what

has been reported for the effect of different additive contents on the textural properties of support materials [43–45].

The catalyst preparation method plays an important role in determining the final textural properties. Roh and co-workers [46] reported a higher surface area, $40 \text{ m}^2 \text{ g}^{-1}$, for a 15 wt% Ni/CeZrO₂ catalyst, compared to the $15 \text{ m}^2 \text{ g}^{-1}$ for the Ni-CeZr in this work. The difference was attributed to the sol-gel preparation method that they applied for catalyst synthesis. Furthermore, Pegios and co-workers [47] synthesized a Ni/Al₂O₃ catalyst using a hard templating on activated carbon method, yielding $162 \text{ m}^2 \text{ g}^{-1}$, which is higher than Ni-Al (see Table 1) synthesized by precipitation (support) and incipient wetness impregnation (catalyst) methods.

3.2. The effect of support

The catalytic carbon gasification mechanism by O₂ was investigated at 993 K for the set of “coked” Ni-based catalysts supported on different materials, Al₂O₃, MgAl₂O₄, MgFe_{0.09}Al_{1.91}O₄ and CeZrO₂. These supports can be distinguished based on extent of their redox functionality. Al₂O₃ and MgAl₂O₄ do not show redox functionality, whereas MgFe_xAl_{2-x}O₄ and CeZrO₂ have good redox properties and oxygen mobility is present [42,48–52].

O₂ pulses were admitted to the coked catalysts. The number of O₂ pulses was not the same for all the studied catalysts as they were continued up to the level where there was CO or CO₂ production. The profiles of O₂ conversion as a function of pulse number are shown in Fig. S2. O₂ conversion was 100% during the first ~100 pulses for all the studied catalysts which can be attributed to different contributions: oxygen uptake by the catalyst, including support and metal oxidation, and oxidation of carbon by gas phase oxygen.

Fig. 1 displays the oxygen uptake ($C_{\text{O,Mi}}$, %) and the conversion of oxygen to gas phase products (C_{COx} , %), CO and CO₂, during the isothermal carbon gasification over different Ni catalysts. The oxygen uptake showed a similar trend for Ni catalysts supported on Al₂O₃ and

MgAl₂O₄, indicating that the same phenomena occur (Fig. 1A and B). Initially, the oxygen uptake is very high, 89% and 97% for Ni-Al and Ni-MgAl respectively, while no CO or CO₂ is formed. The latter implies that oxygen is mainly consumed in the catalyst bed for a process other than carbon gasification, namely oxidation of metal Ni particles to NiO. After that, the oxygen uptake drops, because of the start of the carbon gasification process, which consumes lattice oxygen from NiO. It reaches a minimum after approximately 10 pulses, as the conversion to gas phase products attains a maximum.

From 50 to 100 pulses, the oxygen uptake again reaches a plateau at approximately 95%, for Ni supported on Al₂O₃ (Ni-Al) and MgAl₂O₄ (Ni-MgAl), suggesting that most carbon has been oxidized and fast oxidation of surface Ni to NiO continues. The following drop of oxygen uptake, above 100 pulses, is then attributed to the oxidation of bulk Ni to NiO, which is a diffusion determined process. The small amount of oxygen admitted per pulse ($\sim 10^{-7} \text{ mol/pulse}$) did not allow the complete oxidation of Ni particles after 300 pulses and this is reflected by an oxygen uptake different from zero at the end of the experiment.

In case that supports with redox properties, MgFeAl and CeZr, are used for Ni catalysts, Fig. 1C and D, the oxygen uptake is higher than 95% up to 125 pulses. This is in line with the supports without redox functionality: oxygen interacts with the catalyst, implying the oxidation of Ni to NiO and of the support. Carbon oxidation also takes place, mainly using oxygen from within the support reservoir, and hence not causing a decrease in the oxygen uptake. The lower values of oxygen conversion to gas phase products (C_{COx}) for Ni supported on MgFeAl and CeZr compared to Al and MgAl, are attributed to the different reduction degree of the catalysts prior to coking process.

To further investigate the supports without redox properties, independent molar flow responses of CO as a function of time, during O₂ pulses, are given in Fig. 2(A) for the Ni-Al catalyst. The CO₂ molar flow response during carbon gasification by O₂ (not shown) shows the same trend as that of CO for all the studied catalysts, only the intensity of the response is lower as less CO₂ is being produced (Fig. S3). Independent

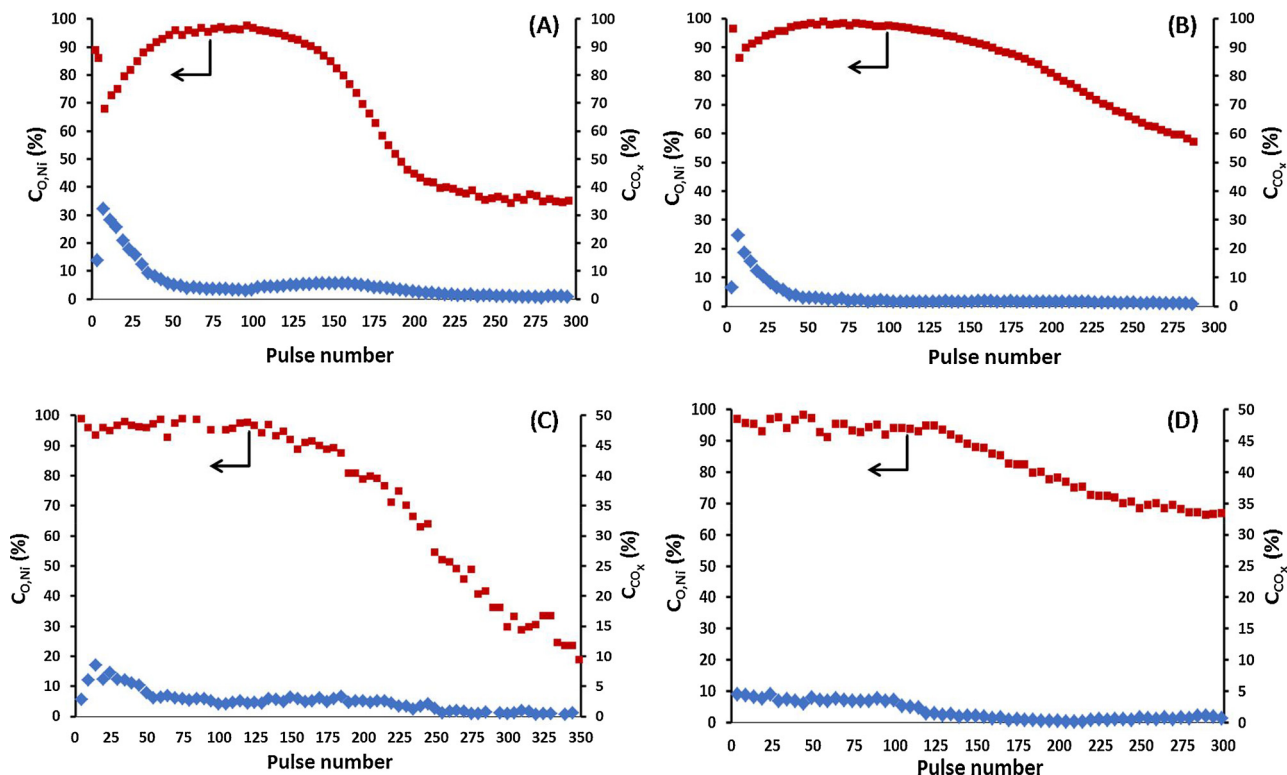


Fig. 1. Oxygen uptake ($C_{\text{O,Mi}}$, %, Eq. (5)) and conversion to gas phase products (C_{COx} , %, Eq. (6)), CO and CO₂, during isothermal O₂ pulses over coked catalysts at 993 K. (A) Ni-Al, (B) Ni-MgAl, (C) Ni-MgFeAl and (D) Ni-CeZr.

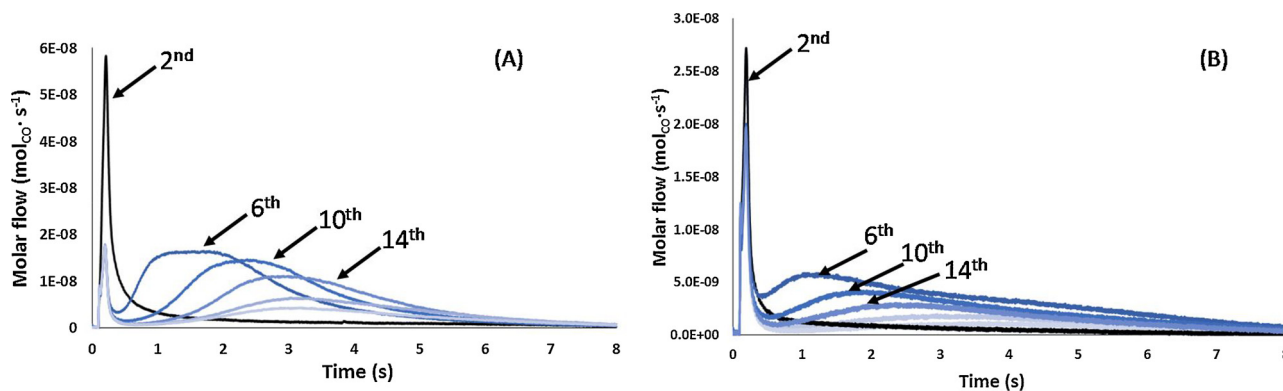


Fig. 2. CO response ($\text{mol}_{\text{CO}} \text{s}^{-1}$) during isothermal O_2 pulses in the TAP reactor at 993 K: pulse numbers 2, 6, 10, 14, 18 and 22 (color going from black over dark blue to light blue). (A): Ni-Al, (B): Ni-MgAl. Ni catalysts were previously coked in a sequence of 420 CH_4 pulses. (For interpretation of the references to colour in this figure legend, the reader is referred to the web version of this article.)

pulses 2, 6, 10, 14, 18 and 22 are depicted in Fig. 2 to show the transient response. For pulse number 2, a sharp peak can be observed at 0.2 s. For the other pulses, the sharp peak at 0.2 s is also visible, but a second more broad peak appears at higher time scales. There is thus a change in CO formation process, implying a time-consuming (or diffusion) process is taking place consecutive to the first CO formation process. Moreover, the maximum of the second broad peak is shifting in time for higher pulse numbers: the maximum is at 1.8 s for pulse number 6, at 2.2 s for pulse 10, at 3.1 s for pulse 14 and at 3.5 s for pulses 18 and 22. The CO response of the very first O_2 pulse is much lower than the response for the next pulses, because oxygen is first being consumed by the catalyst and not by the carbon gasification process.

The same observations can be made for the Ni catalyst supported on MgAl_2O_4 (Fig. 2(B)). Only a sharp peak at 0.2 s is present for pulse number 2, whereas two peaks can be observed for the other pulses: a sharp one at 0.2 s and a more broad peak at higher timescales. The shift in time of this second, broader peak is also visible for this catalyst but the maximum is present at a slightly lower time compared to the Ni-Al catalyst (1.6 s vs. 1.8 s for pulse number 6, 2 s vs. 2.2 s for pulse number 10, 2.8 s vs. 3.1 s for pulse number 14).

The first sharp peak that is observed in Fig. 2(A) and (B), for Ni supported on both Al_2O_3 and MgAl_2O_4 supports, can be attributed to the gasification of carbon that is located close to the active metal (Ni) [13]. However, the total amount of CO and CO_2 that is produced during the first 2–3 pulses is far lower than that of the 4th–18th pulses (Fig. S3), while the inlet O_2 was always completely consumed (Fig. S2). This implies that during the first 2–3 pulses, parallel to the carbon gasification, O_2 was mainly consumed in another process, namely oxidation of Ni to NiO, as indicated by the oxygen uptake in Fig. 1(A) and (B). The process of Ni oxidation is strongly exothermic (Eq. (10)), resulting in a local temperature increase of 50–60 K in total, which brings the catalyst close to the Tamman temperature. In case of NiO and Ni, the Tamman temperatures are equal to 1290 and 1030 K, the latter being only slightly higher than the temperature at which the TAP experiments are performed (993 K). This temperature increase by Ni oxidation provides the necessary energy to start particle migration. As during these first O_2 pulses, the bulk of Ni is not yet oxidized to NiO, due to the small amount of mol per pulse ($\sim 10^{-7}$ mol/pulse), the migrating particles consist mainly of metallic Ni bearing a thin oxide shell.

The migration of Ni particles provides a possible explanation of the development of the second peak in the CO response, observed in Fig. 2. Carbon species which are located away from the active metals can be oxidized after migration of metal particles through their surface oxygen. This migration process is responsible for the shifting in time of the second CO peak. Furthermore, the thermodynamics of carbon oxidation through lattice oxygen of NiO, Eqs. (11) and (12), show that $\Delta_r G^\circ$

is negative at 993 K for both reactions and thus the reaction is favorable at the applied conditions. Particles mobility was previously observed by Gardin and co-workers, using *in-situ* environmental transmission electron microscopy (ETEM) during the oxidation of soot by silver [53]. They concluded that the silver particles exhibited significant mobility during the soot oxidation, and this mobility, which increases the soot/catalyst contact, is expected to be an important factor at lower oxidation temperature.

The CO and CO_2 production that occurs during the first 2–3 pulses could also be attributed to gas-phase interaction of O_2 with the deposited carbon. However, direct carbon gasification only becomes more pronounced at higher temperatures. Theofanidis and co-workers [13] performed O_2 -TPO on graphite and on a spent Ni/MgAl₂O₄ catalyst. The CO_2 intensity peak maximum obtained for pure graphite oxidation (1073 K) lies higher than for carbon species oxidation over Ni (850 K), implying that higher temperatures are required for the direct interaction of carbon species with gas phase O_2 . As the operating temperature during O_2 gasification in the TAP reactor is only 993 K, it is concluded that the deposited carbon species are mainly oxidized by lattice oxygen. However, a contribution coming from direct carbon gasification cannot be neglected and partially contributes to the gasification process.

After this initial part that results in a fast increase of the local temperature by 50–60 K in total, the process continues in two parallel steps: 1) oxidation of Ni to NiO from gas phase O_2 (Eq. (10)), which is strongly exothermic and 2) reduction of NiO according to Eqs. (11) and (12), producing CO and CO_2 , respectively. The contribution of oxygen spillover in carbon gasification is considered negligible: during oxygen pulses the catalyst surface will be oxidized, implying the formation of a negligible amount of surface oxygen, as it reported elsewhere [13].

A similar experiment was performed using MgFeAl and CeZr as supports for the Ni catalyst, in order to examine the effect of support's redox functionality on the carbon gasification mechanism. The CO response during carbon gasification as a function of time for Ni-MgFeAl and Ni-CeZr is given in Fig. 3(A) and (B), respectively. For both catalysts, the same CO response profiles can be observed: only a sharp peak at 0.2 s is present and the peak maximum coincides for all pulses. In particular, there is no second peak, shifting in time as previously observed for Ni-Al and Ni-MgAl (Fig. 2). In this case, the temperature increase per oxygen pulse remains stable and equal to approximately 7 and 12 K/ O_2 pulse for Ni-CeZr and Ni-MgFeAl, respectively.

The different CO response behavior implies that a different CO formation process takes place depending on the catalyst support. The sharp peak at 0.2 s, in case of both catalysts shown in Fig. 4, can be attributed to different contributions: (1) gasification of carbon that is close to the active metal via catalyst lattice oxygen, (2) carbon gasification of distant carbon species via lattice oxygen provided by the support and (3) direct carbon gasification by gas phase O_2 , which

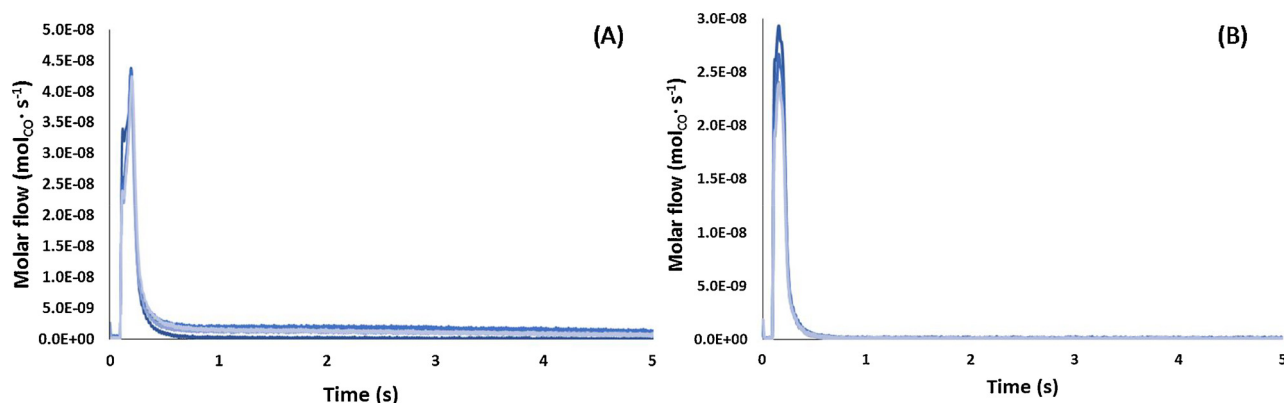


Fig. 3. CO response ($\text{mol}_{\text{CO}} \text{s}^{-1}$) during isothermal O_2 pulses in the TAP reactor at 993 K: pulse numbers 2, 6, 10, 14, 17 and 22 (color going from black over dark blue to light blue). (A): Ni-MgFeAl, (B): Ni-CeZr. Ni catalysts were previously coked in a sequence of 420 CH_4 pulses. (For interpretation of the references to colour in this figure legend, the reader is referred to the web version of this article.)

remains limited because of temperature. Both MgFeAl and CeZr are supports that show high oxygen mobility [36,48,54,55]. This high oxygen mobility is attributed to the presence of oxygen vacancies for CeZr and to the good redox properties of Fe for $\text{MgFe}_x\text{Al}_{2-x}\text{O}_4$. Lattice oxygen provided by the support is consumed during the carbon oxidation step and can be recovered by gas phase O_2 .

3.3. The effect of active metal type and fraction exposed

3.3.1. Fraction exposed

One of the parameters that can affect the carbon gasification rate is the exposed fraction of the active metals. To investigate the dependence of the carbon gasification rate and mechanism on fraction exposed, two different loadings, 1 and 9 wt%, of the same catalyst were compared. The increase of metal loading resulted in a decrease of the metallic Ni fraction exposed, from $21 \pm 3\%$ for 1Ni-MgAl to $9 \pm 1\%$ for Ni-MgAl. The calculation of the Ni fraction exposed for the 1 wt% loading was

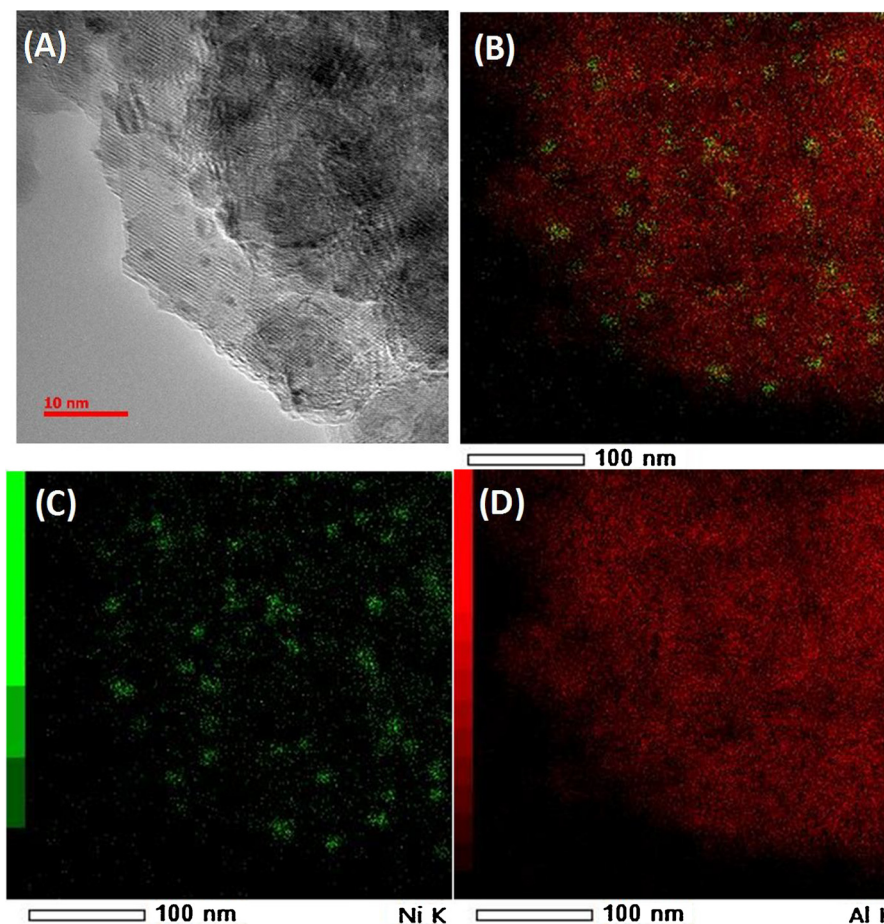


Fig. 4. (A) HRTEM image of reduced 1Ni-MgAl catalyst (1 mL s^{-1} of 32 vol% H_2/Ar using a heating ramp of 15 K min^{-1} up to 1123 K and a dwell time of 30 min). EDX elemental mapping of (A): (B) overlay, (C) Ni and (D) Al.

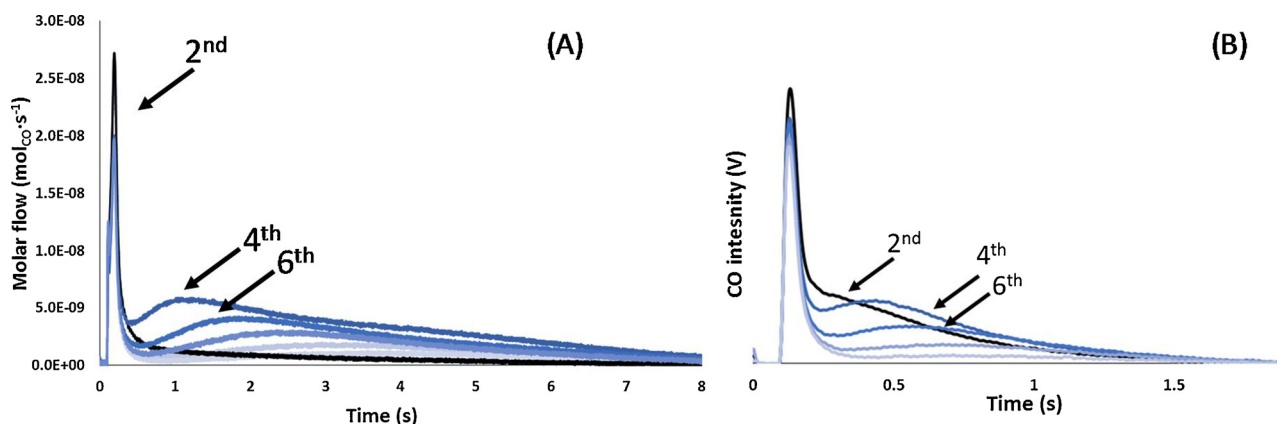


Fig. 5. CO response ($\text{mol}_{\text{CO}} \text{s}^{-1}$) during isothermal O_2 pulses in the TAP reactor at 993 K. (A): Ni-MgAl, (B): 1Ni-MgAl. Ni catalysts were previously coked in a sequence of 420 CH_4 pulses.

based on the HRTEM images (Fig. 4), while in case of Ni-MgAl the value was published elsewhere [36]. Similar results were observed by Li and co-workers [56], who systematically investigated the effect of Ni loading supported on $\alpha\text{-Al}_2\text{O}_3$ for oxidative steam reforming of methane. They found that the number of surface Ni atoms increased in the loading range of 0.2–2.6 wt%, while it remained stable in the range of 2.6–10.6 wt%.

Fig. 5 shows the CO response during carbon oxidation over Ni-MgAl and 1Ni-MgAl at 993 K. The time shift is present for both samples, but it occurs earlier in time (0.5 s to 0.75 s) for 1Ni-MgAl compared to Ni-MgAl (1.8 s to 3.1 s).

Thus, the gasification mechanism for distant carbon occurs in both samples does not depend on the exposed fraction of the active metal. The only difference is originating from the fact that smaller particles start to diffuse earlier than larger ones, following transport between metal particles of metal atoms or small agglomerates (atom migration, Ostwald ripening) [1]. This is reflected in a higher value of the diffusion coefficient (Table 2) in case of 1Ni-MgAl ($6.5 \times 10^{-17} \text{ m}^2 \text{ s}^{-1}$) compared to Ni-MgAl ($2.6 \times 10^{-17} \text{ m}^2 \text{ s}^{-1}$), which can be estimated applying the Einstein equation (Eq. (14)):

$$D = \frac{x^2}{t} \quad (14)$$

where x is half the mean distance between Ni-Ni particles (m) obtained from TEM (Fig. 5), assuming it to be the maximum distance that a particle can travel, t the time shifting (s) of the peak maximum as observed from Fig. 5 and D is the diffusion coefficient ($\text{m}^2 \text{ s}^{-1}$).

3.3.2. Effect of active metal

The type of catalyst used and thus the active metal could also affect the carbon gasification mechanism. Therefore, Ni was compared with a noble metal, Rh, having the same loading (1 wt%) and support material (MgAl_2O_4), in order to determine the influence of the active metal. A similar CO response profile with that of 1 Ni (Fig. 5(B)) was obtained (not shown), where the first sharp peak at 0.2 s is visible for all pulses, while a second, more broad peak can be observed for the following pulses. The CO peak maximum occurs at 0.3 s after 4 pulses and at 0.5 s after 16 pulses for 1 Rh/ MgAl_2O_4 . The presence of the second, broader peak can be attributed to Rh particle migration to distant carbon

Table 2
Estimated diffusion coefficients of Ni particles.

Catalyst	Half mean Ni-Ni distance (nm) ^a	Time (s)	D ($\text{m}^2 \text{ s}^{-1}$)
Ni-MgAl	8.5	2.80	2.6×10^{-17}
1Ni-MgAl	7.0	0.75	6.5×10^{-17}

^a Estimated statistically via 2D projection of HRTEM images.

followed by gasification as was proposed for the Ni-based catalysts. The lower timescales can be explained by the higher metallic Rh exposed fraction ($55 \pm 1\%$) compared to Ni ($21 \pm 3\%$).

However, next to particle migration another contribution is possible for Rh, namely the decomposition reaction of Rh_2O_3 to metallic Rh and oxygen. Rh oxide decomposition is close to equilibrium at 993 K, as indicated in Fig. 6, which displays the Ellington diagram of Rh_2O_3 and NiO. Thus, Rh_2O_3 can decompose to metallic Rh and oxygen, leading to O-species, which can migrate towards the deposited carbon species and oxidize them. For NiO on the other hand, higher temperatures are needed for decomposition, implying the stability of NiO at the applied conditions, so that NiO decomposition as contribution to the reaction mechanism is considered to be negligible.

To examine the metal-oxide stability in more detail and verify our aforementioned hypothesis, O_2 pulse-response experiments were performed in the TAP reactor using Ni and Rh catalysts. The O_2 molar flow was recorded during O_2 pulses on “as-prepared” 1Ni and 1Rh/ MgAl_2O_4 catalysts. The responses over the catalyst beds were compared to that of a quartz bed, which is considered to be inert and thus should not take up oxygen. The results are shown in Figs. S4 and S5, respectively. The outlet O_2 molar flow response for the Ni catalyst bed is similar to that of the quartz bed at 793 K and 993 K, implying that no oxygen uptake occurs in case of 1Ni-MgAl at both examined temperatures. This suggests that NiO remains stable at temperatures around 1000 K and is not decomposed to Ni and oxygen.

The outlet O_2 molar flow responses do differ when applied to the Rh catalyst bed. Fig. S5 shows that the peak maximum of the outlet O_2 molar flow always remains below that of a quartz bed and is increased when decreasing the temperature. This is an indication that Rh_2O_3 decomposes to Rh and oxygen at these temperatures, in agreement with the Ellington diagram (Fig. 6). Fig. S5 can be interpreted using the metal-oxide equilibrium. At 993 K, Rh_2O_3 is less stable than NiO, which means that Rh_2O_3 decomposition will take place when no O_2 is flowing (between two pulses). During O_2 pulses, metallic Rh will be re-oxidized, forming Rh_2O_3 , so that less O_2 is detected in the outlet compared to a quartz bed. At 793 K, Rh_2O_3 is more stable and thus less is decomposed. Next to particles migration, the formation of adsorbed O-species, which can migrate towards the deposited carbon species and oxidize them, is another process that can contribute to carbon gasification mechanism for Rh catalysts. This implies that the catalyst regeneration mechanism, with respect to the removal of carbon deposits, depends on the active metal and the stability of the metal oxides at the applied conditions.

3.4. The effect of the nature of deposited carbon

To investigate the effect of carbon structure on the regeneration mechanism, continuous flow experiments were performed during DRM

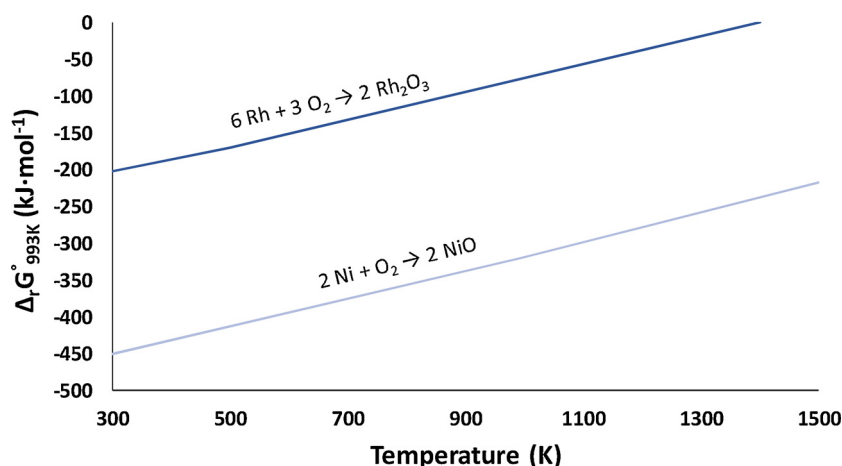


Fig. 6. Ellington diagram of Rh_2O_3 and NiO [57].

at 1023 K, using a CH_4/CO_2 ratio of 2. The higher CH_4 than CO_2 partial pressure led to fast coking of the samples. The deposited carbon was characterized using Raman spectroscopy and HRTEM. Raman spectroscopy can provide information about the electronic properties and detects the presence of ordered carbon species. The G band appearing in the $1500\text{--}1700\text{ cm}^{-1}$ region provides information about the presence of ordered carbon (filamentous or graphitic carbon). It arises from the stretching of the C–C bond in graphitic materials and is common to all sp^2 carbon systems. The Raman spectrum of a single crystal graphene sample shows only one G band at approximately 1581 cm^{-1} Raman shift (depending on the laser wavelength). Here, commercial graphite was used as reference material, which includes two contributions at 1555 and 1580 cm^{-1} Raman shift (bottom line in Fig. S6) [12,58].

The spectra of polycrystalline and imperfect graphite and other types of carbon show an additional peak at about 1350 cm^{-1} , which is called the D band and a peak at 1620 cm^{-1} , corresponding to the D' band [12]. The D band is caused by a disordered structure of graphene. The presence of disorder in sp^2 -hybridized carbon systems results in resonance Raman features, thus making Raman spectroscopy one of the most sensitive techniques to characterize disorder in sp^2 carbon materials [59,60].

The integrated intensity ratio I_D/I_G , for the D and G bands, is often used to characterize the defects in graphitic materials. Based on the Tuinstra and Koenig (TK) law [61], the I_D/I_G ratio varies inversely with the planar microcrystal graphite size (L_a) [62]. Crystalline carbon without defects has a I_D/I_G ratio less than 0.02 [63]. Fan and co-workers [64] showed that by increasing the microcrystal size, L_a , the graphite crystallinity increased, obtaining a Raman spectrum with nothing but the G band when $L_a > 200\text{ nm}$. A similar spectrum was obtained for commercial graphite (bottom line in Fig. S6), where the I_D/I_G ratio approached zero. Table 3 shows the I_D/I_G ratio for the studied samples. The integrated areas were calculated by fitting a multiple peak Gaussian function to the Raman spectrum (an example of the fitting is shown in Fig. S7). The I_D/I_G ratio for all the samples revealed similar

crystallinity with small variations depending on the support. The crystallinity of graphite varies as a function of reaction conditions, i.e. temperature, CH_4/CO_2 ratio and time-on-stream, but for the same applied conditions lower graphite crystallinity was observed for the MgFeAl support compared to pure Al_2O_3 (from approximately 1–0.9, respectively).

The existence of two types of carbon species structures is observed for all the coked catalysts (Fig. S7). The G band of single crystal graphene (1582 cm^{-1}) changed in position and shape, implying the presence of graphitic-like carbon (more graphene layers) [65,66]. The D and D' bands are also observed and attributed to a defective and disordered structure. This can be an amorphous type of carbon species. Guo et al. [12] found similar results, observing amorphous and graphitic-like carbon using Raman spectroscopy on $\text{Ni/MgAl}_2\text{O}_4$ that was coked via CH_4 temperature programmed decomposition.

The structure of the deposited carbon varies depending on the coking process. Carbon filaments or whiskers are formed during coking in a continuous flow experiment (Fig. 7) while carbon is spread over the Ni particles and the support when coked in TAP reactor (see Fig. S8). Furthermore, the amount of deposited carbon differs with the conditions of coking. O_2 pulses were applied on Ni-Al to examine the effect of carbon structure, based on the coking process, on the regeneration mechanism. The amount of CO_2 and CO that is formed during carbon gasification as a function of pulse number is shown in Fig. S9. More O_2 pulses are needed for the gasification of carbon that was deposited under continuous flow compared to coking in TAP (approximately 400 vs. 75 pulses, Figs. S9 vs. S3, respectively), implying that more carbon is deposited during coking in a continuous flow experiment than upon coking in the TAP reactor.

The CO molar flow responses during carbon O_2 -gasification of Ni-Al coked in continuous flow are similar to Fig. 2, including only a sharp peak at 0.2 s of CO_2 for the first pulse (not shown). By increasing the pulse number, a second, broader peak appears and the maximum is shifting in time from 0.7 to 0.95 and 1 s for pulse numbers 10, 75 and 100. After 300 pulses, the second peak disappears, while the first sharp peak at 0.2 s remains with lower intensity. The CO molar flow response is very similar to the one of CO_2 . The first peak is present at 0.3 s and not 0.2 s as for CO_2 . The maximum of the second peak is shifting in time going from 0.7 to 1.2 s from pulse number 1 to 300. The intensity for both peaks is decreasing for higher pulse numbers and after pulse number 300, almost no CO is detected.

When comparing the two coking methods and thus the different carbon structures, one can conclude that the same phenomena are present: a sharp peak at 0.2 s for every pulse number and a broad second peak at higher time scale, which is shifting and eventually decays. This implies that the catalyst regeneration mechanism does not

Table 3

The integrated intensity ratio I_D/I_G for the coked catalysts: Ni-Al, Ni-MgAl and Ni-MgFeAl. Coking was achieved during DRM for 3 h, 1023 K, $\text{CH}_4/\text{CO}_2 = 2/1$, total pressure of 101.3 kPa.

Catalyst	I_D/I_G
Graphite	0.00
Ni-Al	0.88
Ni-MgAl	0.92
Ni-MgFeAl	1.02

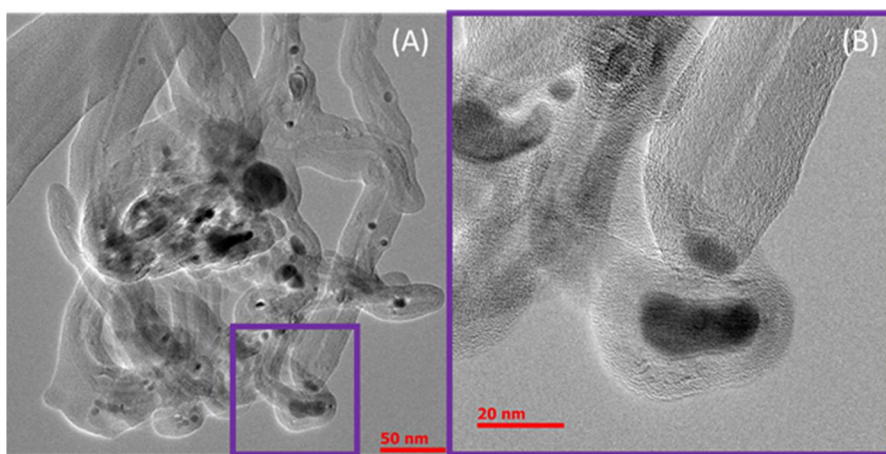


Fig. 7. HRTEM images of the coked Ni-Al sample (after DRM at 1023 K, $\text{CH}_4/\text{CO}_2 = 2/1$, total pressure of 101.3 kPa and reaction time of 3 h). (A) displays tangles of carbon filaments, (B) shows a Ni metal particle in more detail (purple square). Carbon filaments were also formed for Ni-MgAl (not shown).

depend on the type of carbon deposits when oxygen is used as a gasification agent.

3.5. Proposed mechanism

Based on the above-mentioned results, a mechanism for carbon gasification by O_2 is suggested. The features that were considered to affect the mechanism, are: support material, exposed fraction of active metal, type of active metal and structure of deposited carbon. Among them, the exposed fraction of the active metal and the structure of the deposited carbon do not affect the carbon gasification mechanism, but they can affect the rate of carbon removal.

Fig. 8 shows that the catalyst regeneration mechanism strongly depends on the redox properties of the support material. In case that a support without redox functionality is used, such as Al_2O_3 or MgAl_2O_4 , the proposed mechanism consists of two consecutive steps [13]: 1) the Ni metal is oxidized to form NiO, where after the lattice oxygen of the NiO is used to oxidize carbon species that are deposited close to the metals. This results in a local temperature increase, due to the exothermicity of these reactions (oxidation of Ni and carbon), making particles mobile. 2) The nickel oxide particles are migrating towards

carbon deposits located further away, then again oxidizing them via lattice oxygen.

On the other hand, when a support with redox properties is used for Ni catalysts, it also participates in the reaction scheme and the regeneration mechanism consists of two parallel contributions: 1) the Ni metal is oxidized to form NiO, followed by subsequent nearby carbon oxidation via lattice oxygen, 2) carbon removal through lattice oxygen that is provided by the support.

Direct carbon gasification through contact with gas phase oxygen cannot be completely excluded and, if present, will contribute to the first peak that is observed in the TAP experiments at 0.2 s (see Figs. 2 and 3). In addition, the mechanism of carbon bulk diffusion through the metal particles, resulting in dissolved carbon, proposed by Figueiredo and Trimm [9], cannot be excluded. However, a previous publication [13] showed that metal oxide formation proceeds first and afterwards the carbon gasification process starts. To further investigate the involved solid-state reactions, based on Eqs. (11) and (12), proposed as steps for the catalytic carbon gasification mechanism, a mechanical mixture of graphite and NiO powder (weight ratio of approximately 1:1) was subjected to a temperature programmed treatment under inert environment (He). Fig. 9 displays the 2D in-situ XRD pattern of the

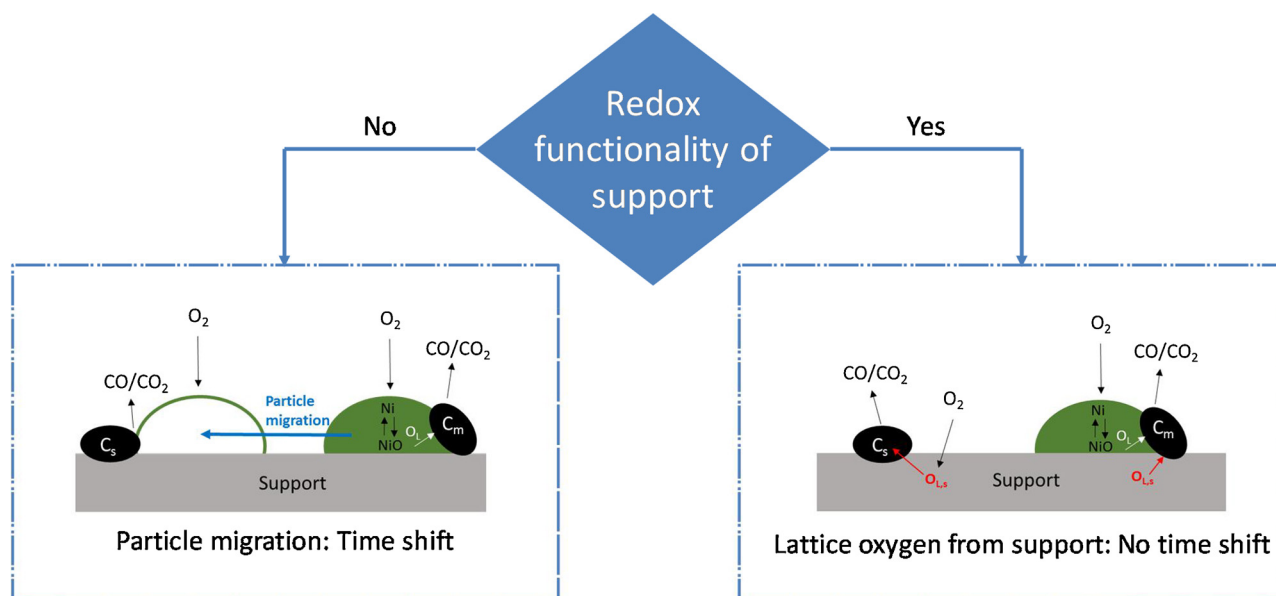


Fig. 8. Schematic representation of isothermal catalyst regeneration as a function of support redox functionality. C_m : carbon deposited on metals, C_s : carbon deposited far from metals, O_s : surface oxygen, O_L : lattice oxygen. The carbon illustration does not represent the actual carbon structure.

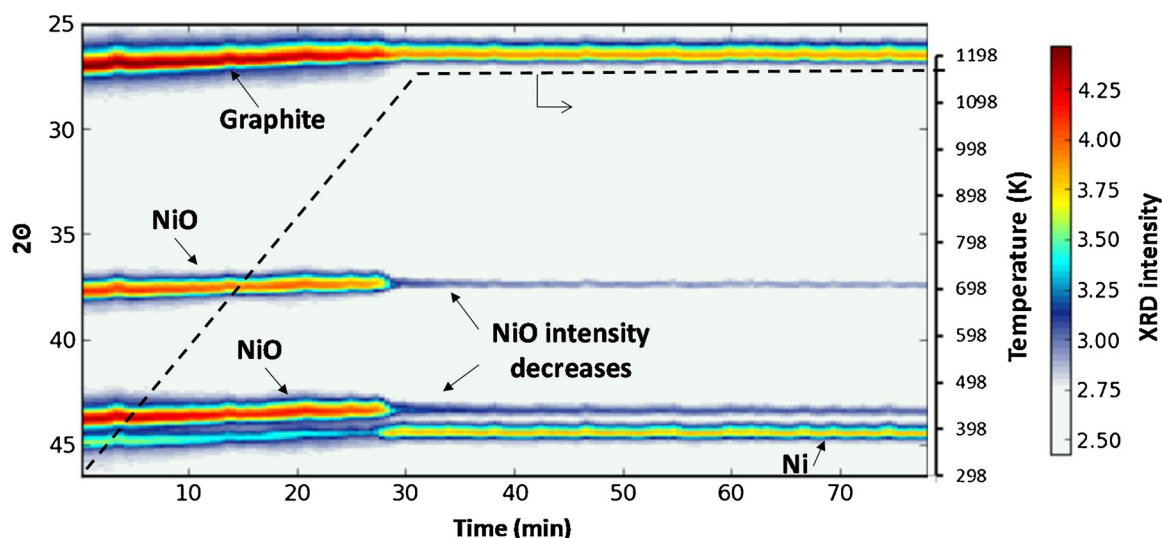


Fig. 9. 2D in-situ XRD pattern during temperature programmed treatment of a mechanical mixture, consisting of graphite and NiO (weight ratio 1:1), under inert environment (He). Heating ramp of 30 K/min, maximum temperature 1173 K, dwell time at 1173 K equal to 45 min.

mechanical mixture during the treatment. A 2θ diffraction angles window was selected in order to follow the evolution of graphite, NiO and metallic Ni diffraction peaks. Before the treatment NiO and graphite diffraction peaks are present (Fig. S10). From the decreased intensities of graphite and NiO diffractions and the appearance of metallic Ni diffraction peaks around ~ 1073 K, NiO lattice oxygen was consumed for graphite oxidation, reducing it to metallic Ni. The graphite peak is still present after the treatment (Figs. 9 and S10), as it was not completely oxidized. Clearly, solid-state reactions between bulk NiO and graphite can take place at elevated temperatures, thus participating in the reaction scheme. At steady-state conditions, the rates of NiO reduction via Eqs. (11) and (12) and Ni oxidation from gas phase oxygen are similar, following a Mars-van Krevelen (or redox) mechanism [68]. Furthermore, the thermodynamics of Eqs. (11) and (12) show that the ΔG° of these reactions are negative at 993 K. Hence, it is likely that the formation of metal oxides will not allow diffusion of carbon through the particle, but rather carbon will be oxidized at the contact points with the oxide (Figs. 9 and S10).

Finally, the type of active metal can affect the catalyst regeneration mechanism depending on the stability of metal oxides at the applied conditions. In case the metal oxide is not stable (see § 3.3: type of active metal), apart from particle migration, oxygen spillover can also contribute to the carbon oxidation.

4. Conclusions

A set of supports was prepared by one-pot synthesis including: Al_2O_3 , MgAl_2O_4 , $\text{MgFe}_{0.09}\text{Al}_{1.91}\text{O}_4$ and CeZrO_2 in order to investigate the regeneration mechanism of Ni catalysts. The aforementioned support materials were categorized according to their redox properties. Al_2O_3 and MgAl_2O_4 do not show redox properties, in contrast to $\text{MgFe}_{0.09}\text{Al}_{1.91}\text{O}_4$ and CeZrO_2 , which have good redox properties and show oxygen mobility.

A TAP reactor was used to investigate the isothermal carbon species gasification process at 993 K. A different mechanism was concluded for Ni catalysts depending on the used support material. In case of supports without redox properties, the mechanism consists of two consecutive contributions. First, the metallic Ni is oxidized to form NiO, resulting in a local temperature increase of 50–60 K. The raised local temperature ensures metal particle migration to carbon that was deposited away from the metal and subsequently oxidation via lattice oxygen. After this initial part, the oxidation of Ni to NiO from gas phase O_2 and the reduction of NiO during carbon oxidation to produce CO and CO_2 , are

parallel processes.

On the other hand, the mechanism of Ni catalyst regeneration on supports with redox properties is proposed to consist of two parallel contributions: 1) Ni metal is oxidized to form NiO, where after lattice oxygen of NiO is used for the oxidation of carbon that is deposited on the metals, 2) carbon oxidation through lattice oxygen that is provided by the support. No particle migration takes place in this case. The temperature increase remains stable and equal to approximately 7 and 12 K/ O_2 pulse for Ni/CeZr and Ni/MgFeAl, respectively.

Finally, no dependency of the carbon gasification mechanism on the exposed fraction (particle size) and on the type of active metal was observed. However, an additional contribution, next to particle migration, can be possible for noble metals, such as Rh, as Rh_2O_3 decomposition to metallic Rh and adsorbed O-species is close to equilibrium around 993 K. The adsorbed O-species can migrate towards deposited carbon (O_2 -spillover) and give rise to its oxidation.

Acknowledgments

This work was supported by the FAST industrialization by Catalyst Research and Development (FASTCARD) project, which is a Large Scale Collaborative Project supported by the European Commission in the 7th Framework Programme (GA no 604277) and by the “Long Term Structural Methusalem Funding by the Flemish Government”. The authors acknowledge support from Lukas Buelens (Laboratory for Chemical Technology, Department of Engineering and Architecture, Ghent University) for the HRTEM measurements.

Appendix A. Supplementary data

Supplementary material related to this article can be found, in the online version, at doi:<https://doi.org/10.1016/j.apcatb.2018.08.042>.

References

- [1] J.R. Rostrup-Nielsen, L.J. Christiansen (Eds.), *Concepts in Syngas Manufacture*, I.C. Press, 2011.
- [2] J.-W. Snoeck, G. Froment, M. Fowles, Filamentous carbon formation and gasification: thermodynamics, driving force, nucleation, and steady-state growth, *J. Catal.* 169 (1997) 240–249.
- [3] D. Brown, J. Clark, A. Foster, J. McCarroll, M. Sims, *Inhibition of Coke Formation in Ethylene Steam Cracking*, ACS Publications, 1982.
- [4] L.S. Lobo, J.L. Figueiredo, C.A. Bernardo, Carbon formation and gasification on metals. Bulk diffusion mechanism: a reassessment, *Catal. Today* 178 (2011) 110–116.

- [5] M. Argyle, C. Bartholomew, Heterogeneous catalyst deactivation and regeneration: a review, *Catalysts* 5 (2015) 145.
- [6] L.S. Lobo, Intrinsic kinetics in carbon gasification: understanding linearity, “nano-worms” and alloy catalysts, *Appl. Catal. B: Environ.* 148–149 (2014) 136–143.
- [7] L.S. Lobo, Catalytic carbon gasification: review of observed kinetics and proposed mechanisms or models—highlighting carbon bulk diffusion, *Catal. Rev.* 55 (2013) 210–254.
- [8] J.M. Kanervo, A.O.I. Krause, J.R. Aittamaa, P.H. Hagelberg, K.J.T. Lipiäinen, I.H. Eilos, J.S. Hiltunen, V.M. Niemi, Kinetics of the regeneration of a cracking catalyst derived from TPO measurements, *Chem. Eng. Sci.* 56 (2001) 1221–1227.
- [9] J.L. Figueiredo, D.L. Trimm, Gasification of carbon deposits on nickel catalysts, *J. Catal.* 40 (1975) 154–159.
- [10] A. Tomita, Y. Tamai, Hydrogenation of carbons catalyzed by transition metals, *J. Catal.* 27 (1972) 293–300.
- [11] A. Tomita, Catalysis of carbon–gas reactions, *Catal. Surv. Jpn.* 5 (2001) 17–24.
- [12] J. Guo, H. Lou, X. Zheng, The deposition of coke from methane on a Ni/MgAl₂O₄ catalyst, *Carbon* 45 (2007) 1314–1321.
- [13] S.A. Theofanidis, R. Batchu, V.V. Galvita, H. Poelman, G.B. Marin, Carbon gasification from Fe–Ni catalysts after methane dry reforming, *Appl. Catal. B* 185 (2016) 42–55.
- [14] N. Zong, Y. Liu, Learning about the mechanism of carbon gasification by CO₂ from DSC and TG data, *Thermochim. Acta* 527 (2012) 22–26.
- [15] D. Pakhare, J. Spivey, A review of dry (CO₂) reforming of methane over noble metal catalysts, *Chem. Soc. Rev.* 43 (2014) 7813–7837.
- [16] T.H. Gardner, J.J. Spivey, E.L. Kugler, D. Pakhare, CH₄–CO₂ reforming over Ni-substituted barium hexaaluminate catalysts, *Appl. Catal. A* 455 (2013) 129–136.
- [17] W. Gac, A. Denis, T. Borowiecki, L. Kepiński, Methane decomposition over Ni–MgO–Al₂O₃ catalysts, *Appl. Catal. A* 357 (2009) 236–243.
- [18] A.S.A. Al-Fatih, A.A. Ibrahim, A.H. Fakeeha, M.A. Soliman, M.R.H. Siddiqui, A.E. Abasaheed, Coke formation during CO₂ reforming of CH₄ over alumina-supported nickel catalysts, *Appl. Catal. A* 364 (2009) 150–155.
- [19] C.A. Querini, S.C. Fung, Coke characterization by temperature programmed techniques, *Catal. Today* 37 (1997) 277–283.
- [20] K.M. Hardiman, C.G. Cooper, A.A. Adesina, R. Lange, Post-mortem characterization of coke-induced deactivated alumina-supported Co–Ni catalysts, *Chem. Eng. Sci.* 61 (2006) 2565–2573.
- [21] H.S. Taylor, H.A. Neville, Catalysis in the interaction of carbon with steam and with carbon dioxide, *J. Am. Chem. Soc.* 43 (1921) 2055–2071.
- [22] F.H. Franke, M. Meraikib, Die katalytische Wirkung von Alkalien auf die vergasungsreaktion des kohlenstoffs, *Carbon* 8 (1970) 423–433.
- [23] B.J. Wood, K.M. Sancier, The mechanism of the catalytic gasification of coal char: a critical review, *Catal. Rev.* 26 (1984) 233–279.
- [24] C.A. Bernardo, D.L. Trimm, The kinetics of gasification of carbon deposited on nickel catalysts, *Carbon* 17 (1979) 115–120.
- [25] E. Baumgarten, A. Schuck, Oxygen spillover and its possible role in coke burning, *Appl. Catal.* 37 (1988) 247–257.
- [26] F. Kapteijn, Kinetics of catalysed and uncatalysed coal gasification, in: J.A. Moulijn, J. Figueiredo, J. Moulijn (Eds.), *Carbon and Coal Gasification*, Springer, Netherlands, 1986, pp. 291–360.
- [27] D. Fino, N. Russo, C. Badini, G. Saracco, V. Specchia, Effect of active species mobility on soot-combustion over Cs–V catalysts, *AIChE J.* 49 (2003) 2173–2180.
- [28] B.R. Stanmore, V. Tschamber, J.F. Brilhac, Oxidation of carbon by NO_x with particular reference to NO₂ and N₂O, *Fuel* 87 (2008) 131–146.
- [29] J. Thomas, P. Walker Jr, Mobility of metal particles on a graphite substrate, *J. Chem. Phys.* 41 (1964) 587–588.
- [30] D. McKee, The copper-catalyzed oxidation of graphite, *Carbon* 8 (1970) 131IN3137–3136IN8139.
- [31] D. Gardini, J.M. Christensen, C.D. Damsgaard, A.D. Jensen, J.B. Wagner, Visualizing the mobility of silver during catalytic soot oxidation, *Appl. Catal. B: Environ.* 183 (2016) 28–36.
- [32] T.J. Booth, F. Pizzocchero, H. Andersen, T.W. Hansen, J.B. Wagner, J.R. Jinschek, R.E. Dunin-Borkowski, O. Hansen, P. Boggild, Discrete dynamics of nanoparticle channelling in suspended graphene, *Nano Lett.* 11 (2011) 2689–2692.
- [33] A. Tomita, Y. Tamai, Optical microscopic study on the catalytic hydrogenation of graphite, *J. Phys. Chem.* 78 (1974) 2254–2258.
- [34] R. Baker, The relationship between particle motion on a graphite surface and Tammann temperature, *J. Catal.* 78 (1982) 473–476.
- [35] L.S. Lobo, S.A.C. Carabineiro, Kinetics and mechanism of catalytic carbon gasification, *Fuel* 183 (2016) 457–469.
- [36] J.T. Gleaves, G. Yablonsky, X. Zheng, R. Fushimi, P.L. Mills, Temporal analysis of products (TAP)—recent advances in technology for kinetic analysis of multi-component catalysts, *J. Mol. Catal. A: Chem.* 315 (2010) 108–134.
- [37] U. Menon, V.V. Galvita, G.B. Marin, Reaction network for the total oxidation of toluene over CuO–CeO₂/Al₂O₃, *J. Catal.* 283 (2011) 1–9.
- [38] R. Batchu, V.V. Galvita, K. Alexopoulos, K. Van der Borgh, H. Poelman, M.-F. Reyniers, G.B. Marin, Role of intermediates in reaction pathways from ethene to hydrocarbons over H-ZSM-5, *Appl. Catal. A: Gen.* 538 (2017) 207–220.
- [39] S.A. Theofanidis, V.V. Galvita, H. Poelman, N.V.R.A. Dharanipragada, A. Longo, M. Meledina, G. Van Tendeloo, C. Detavernier, G.B. Marin, Fe-containing magnesium aluminate support for stability and carbon control during methane reforming, *ACS Catal.* 8 (2018) 5983–5995.
- [40] S. Theofanidis, V. Galvita, C. Konstantopoulos, H. Poelman, G. Marin, Fe-based nano-materials in catalysis, *Materials* 11 (2018) 831.
- [41] S. Rossignol, F. Gerard, D. Duprez, Effect of the preparation method on the properties of zirconia-ceria materials, *J. Mater. Chem.* 9 (1999) 1615–1620.
- [42] J. Kašpar, P. Fornasiero, M. Graziani, Use of CeO₂-based oxides in the three-way catalysis, *Catal. Today* 50 (1999) 285–298.
- [43] J. Gleaves, J. Ebner, T. Kuechler, Temporal analysis of products (TAP)—a unique catalyst evaluation system with submillisecond time resolution, *Catal. Rev. Sci. Eng.* 30 (1988) 49–116.
- [44] J.T. Gleaves, G.S. Yablonskii, P. Phanawadee, Y. Schuurman, TAP-2: an interrogative kinetics approach, *Appl. Catal. A: Gen.* 160 (1997) 55–88.
- [45] N.V.R.A. Dharanipragada, L.C. Buelens, H. Poelman, E. De Grave, V.V. Galvita, G.B. Marin, Mg–Fe–Al–O for advanced CO₂ to CO conversion: carbon monoxide yield vs. oxygen storage capacity, *J. Mater. Chem. A* 3 (2015) 16251–16262.
- [46] C. Shi, P. Zhang, Role of MgO over γ-Al₂O₃-supported Pd catalysts for carbon dioxide reforming of methane, *Appl. Catal. B* 170–171 (2015) 43–52.
- [47] S.A. Theofanidis, V.V. Galvita, H. Poelman, G.B. Marin, Enhanced carbon-resistant dry reforming Fe–Ni catalyst: role of Fe, *ACS Catal.* 5 (2015) 3028–3039.
- [48] S. Damyanova, B. Pawelec, K. Arishtirova, J.L.G. Fierro, Biogas reforming over bimetallic PdNi catalysts supported on phosphorus-modified alumina, *Int. J. Hydrogen Energy* 36 (2011) 10635–10647.
- [49] H.-S. Roh, K.-W. Jun, W.-S. Dong, S.-E. Park, Y.-S. Baek, Highly stable Ni catalyst supported on Ce–ZrO₂ for oxy-steam reforming of methane, *Catal. Lett.* 74 (2001) 31–36.
- [50] N. Pegios, V. Bliznuk, S.A. Theofanidis, V.V. Galvita, G.B. Marin, R. Palkovits, K. Simeonov, Ni nanoparticles and the Kirkendall effect in dry reforming of methane, *Appl. Surf. Sci.* 452 (2018) 239–247.
- [51] E.C. Vagia, A.A. Lemonidou, Investigations on the properties of ceria–zirconia-supported Ni and Rh catalysts and their performance in acetic acid steam reforming, *J. Catal.* 269 (2010) 388–396.
- [52] S. Damyanova, B. Pawelec, K. Arishtirova, M.V.M. Huerta, J.L.G. Fierro, The effect of CeO₂ on the surface and catalytic properties of Pt/CeO₂–ZrO₂ catalysts for methane dry reforming, *Appl. Catal. B* 89 (2009) 149–159.
- [53] S.M. de Lima, I.O. da Cruz, G. Jacobs, B.H. Davis, L.V. Mattos, F.B. Noronha, Steam reforming, partial oxidation, and oxidative steam reforming of ethanol over Pt/CeZrO₂ catalyst, *J. Catal.* 257 (2008) 356–368.
- [54] L.V. Mattos, F.B. Noronha, Partial oxidation of ethanol on supported Pt catalysts, *J. Power Sources* 145 (2005) 10–15.
- [55] N.V.R.A. Dharanipragada, V.V. Galvita, H. Poelman, L.C. Buelens, G.B. Marin, A. Longo, Insight in kinetics from pre-edge features using time resolved in situ XAS, *AIChE J.* (2017) 1339–1349.
- [56] D. Gardini, J.M. Christensen, C.D. Damsgaard, A.D. Jensen, J.B. Wagner, Visualizing the mobility of silver during catalytic soot oxidation, *Appl. Catal. B* 183 (2016) 28–36.
- [57] N. Laosiripojana, S. Assabumrungrat, Catalytic dry reforming of methane over high surface area ceria, *Appl. Catal. B* 60 (2005) 107–116.
- [58] A. Horváth, G. Stefler, O. Geszti, A. Kieneman, A. Pietraszek, L. Guzzi, Methane dry reforming with CO₂ on CeZr-oxide supported Ni, NiRh and NiCo catalysts prepared by sol–gel technique: relationship between activity and coke formation, *Catal. Today* 169 (2011) 102–111.
- [59] B. Li, K. Maruyama, M. Nurunnabi, K. Kunitomi, K. Tomishige, Effect of Ni loading on catalyst bed temperature in oxidative steam reforming of methane over α-Al₂O₃-supported Ni catalysts, *Ind. Eng. Chem. Res.* 44 (2005) 485–494.
- [60] A. Morteza, The Influence of Atmosphere on Oxides Crystal Growth, *Modern Aspects of Bulk Crystal and Thin Film Preparation*, Intechopen, 2012.
- [61] L. Bokobza, J.-L. Bruneel, M. Couzi, Raman spectra of carbon-based materials (from graphite to carbon black) and of some silicone composites, *J. Carbon Res.* 1 (2015) 77–94.
- [62] A. Maghsoumi, L. Brambilla, C. Castiglioni, K. Müllen, M. Tommasini, Overtone and combination features of G and D peaks in resonance Raman spectroscopy of the C78H26 polycyclic aromatic hydrocarbon, *J. Raman Spectrosc.* 46 (2015) 757–764.
- [63] M.A. Pimenta, G. Dresselhaus, M.S. Dresselhaus, L.G. Cancado, A. Jorio, R. Saito, Studying disorder in graphite-based systems by Raman spectroscopy, *Phys. Chem. Chem. Phys.* 9 (2007) 1276–1290.
- [64] F. Tuinstra, J.L. Koenig, Raman spectrum of graphite, *J. Chem. Phys.* 53 (1970) 1126.
- [65] A.C. Ferrari, J. Robertson, Interpretation of Raman spectra of disordered and amorphous carbon, *Phys. Rev. B* 61 (2000) 14095–14107.
- [66] J. Maultzsch, C. Thomsen, Characterization of Carbon Nanotubes by Optical Spectroscopy, *Carbon Nanotube Devices*, Wiley-VCH Verlag GmbH & Co. KGaA, 2008, pp. 125–180.
- [67] M.S. Dresselhaus, G. Dresselhaus, R. Saito, A. Jorio, Raman spectroscopy of carbon nanotubes, *Phys. Rep.* 409 (2005) 47–99.

Further reading

- F. Fan, Z. Feng and C. Li, *Raman and UV-Raman Spectroscopies, Characterization of Solid Materials and Heterogeneous Catalysts*, 2012, Wiley-VCH Verlag GmbH & Co. KGaA, 49–87.
- M.S. Dresselhaus, A. Jorio, M. Hofmann, G. Dresselhaus and R. Saito, Perspectives on carbon nanotubes and graphene raman spectroscopy, *Nano Lett.* 10, 2010, 751–758.
- C. Doornkamp and V. Ponec, The universal character of the Mars and Van Krevelen mechanism, *J. Mol. Catal. A: Chem.* 162, 2000, 19–32.
- E.J. Grootendorst and V. Ponec, The Mars and van Krevelen mechanism for oxidation reactions used for a selective reduction reaction—influence of surface OH – groups on the selectivity, In: M. Guisnet, J. Barbier, J. Barrault, C. Bouchoule, D. Duprez, G. Pérot and C. Montassier, (Eds.), *Stud. Surf. Sci. Catal.*, 1993, Elsevier, 487–494.